Nanoscale Advances

ROYAL SOCIETY OF CHEMISTRY

PAPER

View Article Online
View Journal | View Issue

Cite this: *Nanoscale Adv.*, 2024, **6**, 4865

Development of a laser induced graphene (LIG) and polylactic acid (PLA) shape memory polymer composite with simultaneous multi-stimuli response and deformation self-sensing characteristics†

Reza Gholami,[a] Ibrahim Lawan,[a] Panuwat Luengrojanakul,[a] Sahar Ebrahimi,[a] Cheol-Hee Ahn[b] and Sarawut Rimdusit *[a]

This study presents the integration of laser-induced graphene (LIG) on a polylactic acid (PLA) substrate to create a novel shape memory polymer composite (SMPC) with multi-stimuli response and deformation self-sensing characteristics. The LIG was initially engraved on a commercial polyimide film and subsequently transferred to the PLA substrate through hot compression. Raman spectra analysis confirmed the successful engraving of the LIG, exhibiting the typical characteristic peaks. Durability tests revealed that the transferred LIG adhered well to the PLA substrate. Additionally, the transferred LIG demonstrated a sheet resistance of 40.3 Ω sq^{-1}, which facilitated the electrical actuation of the LIG/PLA composite through Joule heating, allowing precise temperature control by manipulating the applied electrical power. An optimum electrical power of 0.95 W was identified to rapidly reach the actuation temperature without exceeding 80 °C. The study also demonstrated the LIG/PLA composite's responsiveness to infrared (IR) light, attributed to photothermal conversion behavior of LIG. An optimum IR intensity of 85 mW cm^{-2} was established for reaching the actuation temperature without surpassing 80 °C. This multi-stimulus functionality was achieved alongside real-time monitoring of the shape recovery ratio, enabled by the piezoresistive properties of LIG, which allowed for recording electrical resistance changes during recovery. This approach eliminates the need for external components and offers a straightforward fabrication process. The ability to actuate and sense deformation using a single, integrated LIG pattern opens new opportunities for developing advanced, multi-responsive, and self-sensing shape memory polymer composites.

Received 30th May 2024
Accepted 30th July 2024

DOI: 10.1039/d4na00450g

rsc.li/nanoscale-advances

1. Introduction

Shape memory polymers (SMPs) are a class of smart materials renowned for their ability to undergo programmed shape changes.[1] This remarkable property allows SMPs to be deformed into a temporary shape under external force and subsequently recover their original, permanent form upon exposure to a specific external trigger,[2] such as heat,[3] electric,[4] light,[5,6] magnetic field,[7] ultrasound,[8] or pH.[9] This inherent property has gained attention in material research, with vast potential applications in diverse fields including aerospace,[10,11] soft-robotics,[12,13] and medical devices.[14,15] Among the various triggering mechanisms, thermally activated shape memory is particularly well-established. Programming for heat-responsive SMPs usually involves a two-step process, firstly, deformation above the glass transition temperature (T_g) with an external force, followed by cooling below T_g to "fix" the temporary shape. Upon heating above T_g again, this fixed shape returns to the original form. Therefore, achieving efficient, localized, and controllable heating becomes crucial for successful actuation of thermally responsive SMPs.

While conventional external heating sources exist, alternative methods offer advantages when direct heating is impractical. These include light (IR radiation) and electric current (Joule heating). Electrically conductive nanofillers, such as carbon nanotubes (CNTs)[16,17] or graphene nanoplatelets (GNPs),[18] and conductive reinforcements like carbon fibers[19] have been incorporated into SMPs to create shape memory polymer composites (SMPC) responsive to electrical actuation. These conductive materials allow internal heat generation

[a]*Center of Excellence in Polymeric Materials for Medical Practice Devices, Department of Chemical Engineering, Faculty of Engineering, Chulalongkorn University, Bangkok, 10330, Thailand. E-mail: sarawut.r@chula.ac.th*

[b]*Department of Materials Science and Engineering, Seoul National University, Seoul 08826, Korea*

† Electronic supplementary information (ESI) available. See DOI: https://doi.org/10.1039/d4na00450g

through Joule heating when an electric current is applied. Similarly, light-responsive SMPCs utilize nanofillers with photothermal conversion capabilities, such as graphene,[20,21] carbon black,[22] CNT,[23] or titanium nitride (TiN).[24,25] These nanofillers enable contactless heat generation for triggering shape recovery of SMPCs. However, incorporating these conductive or photothermal fillers can impact the shape memory performance and other properties of the SMP nanocomposite, whether positive or negative. This necessitates additional experimentation and optimization for any new SMP-filler combination and application.

An ideal scenario would involve an integrated heating source within the SMP that minimally affects its shape memory performance and other physical properties. This is precisely where laser induced graphene (LIG) emerges as a potential solution. LIG is a three-dimensional porous network of graphene flakes exhibiting high electrical conductivity.[26] It's fabricated through a direct-write laser scribing process using a CO_2 laser cutter, commonly found in machine shops. Polyimide (PI) is the most widely used precursor material for LIG synthesis.[27] This technique allows for precise patterning of desired geometries on the substrate. By optimizing laser parameters, researchers can control the formation of LIG with various morphologies and conductivities.[28,29] The exceptional conductivity of LIG has been successfully used for applications requiring resistive Joule heating.[30–32] Previous studies have also shown that LIG exhibits outstanding photothermal conversion capabilities.[33–35] Interestingly, LIG patterns after engraving on PI film can be seamlessly transferred onto diverse polymer substrates.[36,37] Therefore, this transferability suggests that by integrating an LIG pattern onto an SMP substrate, the resulting SMPC can have both resistive Joule heating and photothermal conversion functionalities and can be responsive to both electrical and IR light actuations. Additionally, LIG possesses remarkable piezoresistive properties due to its microporous, foam-like structure, making it suitable for strain sensing applications.[38,39] Beyond triggering shape recovery through Joule heating or photothermal conversion, LIG's piezoresistive nature can add another exciting functionality which is real-time monitoring of the SMPC's deformation during recovery. Despite these compelling attributes, there appears to be a lack of existing research exploring the use of LIG as a multifunctional element for SMPC applications.

Motivated by the promising properties of LIG, this research investigates its potential as a multifunctional component for SMPCs. Polylactic acid (PLA), a well-known bio-based and biodegradable polymer with good shape memory properties,[40] was chosen as the SMP substrate. To explore each LIG functionality, a LIG pattern was first designed. Following preparation through laser engraving on a PI film, the LIG pattern was then transferred onto the PLA substrate using a simple compression technique during hot compression molding to produce an LIG/PLA composite. The transferred LIG and LIG/PLA composite were characterized using various techniques, including Raman spectroscopy, sheet resistance measurements, morphological analysis, adhesion durability tests, and dynamic mechanical analysis (DMA). Subsequently, the Joule heating and photothermal conversion performance of the transferred LIG were systematically investigated to determine the optimal electric power and light intensity needed to achieve the desired actuation temperature of the LIG/PLA composite. Finally, the deformation self-sensing capability of the LIG/PLA composite during shape recovery, actuated by optimal Joule heating and IR light, was examined.

2. Materials and methods

2.1. Materials

The polylactic acid (PLA 4043D) used in the study as a substrate for the shape memory was obtained from Natureworks Co. Ltd and commercial polyimide Kapton® film (125 μm thick) was used for the production of the laser induced graphene (LIG).

2.2. Production of the LIG with the U-shape pattern

The U-shaped LIG pattern with dimensions as shown in Fig. 1(a) was engraved on a commercial grade polyimde (PI) film using a commercial CO_2 laser machine (Trotec Speedy 100, 1.5″ lens). The machine was operated at 4.8 W, 14.4 cm s^{-1}, 500 DPI × 1000 PPI for the power, engraving speed, resolution, respectively, with a 3 mm defocusing distance below the focal plane.

2.3. Transferring the produced U-shape patterned LIG on to a PLA substrate to form the composite

The PLA pellets were dried in an oven at 80 °C for 24 hours. Then, a metal mold was used for compression molding. First,

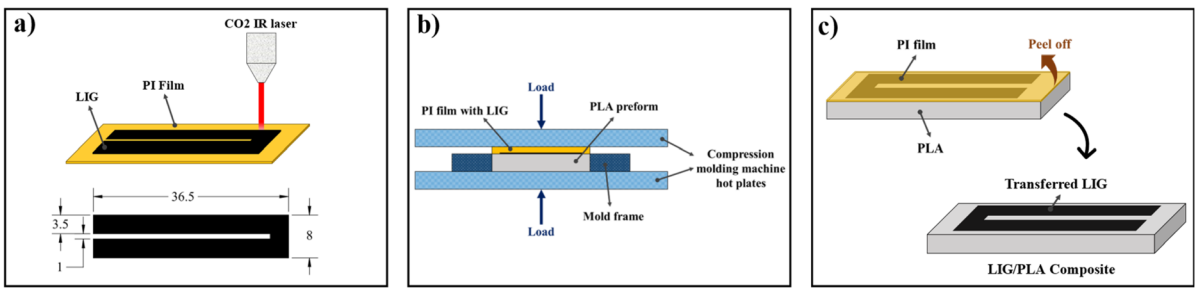

Fig. 1 Schematic illustration of the fabrication process for LIG/PLA composite specimens: (a) production of the LIG with the U-shape pattern on PI film. (b) Transfer of the LIG pattern to a PLA substrate during hot compression molding. (c) Peeling of the PI film.

PLA pellets were poured into the mold cavities (dimensions: 50 × 10 × 1 mm^3) and melted in a vacuum oven at 180 °C to form a void-free PLA preform. The melted PLA preform was then taken out of the vacuum oven, and the PI/LIG film was placed on the top of the molten PLA preform and was then compressed using a hot compression molding machine at 180 °C for 1 minute (Fig. 1(b)). Afterward, the pressure was released, and the mold was allowed to cool down to room temperature. Finally, as shown in Fig. 1(c), the PI film was peeled off from the surface of the PLA transferring the LIG pattern onto the PLA surface to produce the LIG/PLA composite specimens.

2.4. Characterization of the LIG/PLA composites

2.4.1. Raman spectroscopy analysis. Raman spectroscopy was employed to characterize the LIG before and after transferring to PLA substrate. The measurements were performed using a Raman spectrometer model Horiba LabRAM HR Evolution system equipped with a 532 nm laser source with 50× objective lens.

2.4.2. Morphological analysis. The morphology of the LIG film was investigated using scanning electron microscopy JEOL model JSM-6510A(SEM) to characterize its microstructure before and after transfer from the PI film to PLA substrate. SEM was employed at an accelerating voltage of 5 kV. Prior to SEM analysis, the samples were sputter-coated with a thin layer of gold to enhance their electrical conductivity.

2.4.3. Electrical resistance measurements. A four-probe method, utilizing a Jandel RM3 station, was employed to assess the sheet resistance of LIG before and after transferring to PLA. Sheet resistance was calculated for multiple locations on each sample, and the average value was reported.

2.4.4. Adhesion durability of LIG on PLA substrate. To assess adhesion between the LIG and the SMP surface, a peel-off scotch tape test was conducted. The tape was firmly sticked onto the surface and then peeled off in consecutive cycles. The adhesion strength of the LIG was evaluated qualitatively by visually inspecting the peeled tape surface for any LIG particles transferred from the SMP/LIG surface. Additionally, the electrical resistance of the LIG pattern was measured after each peeling cycle to quantitatively assess the adhesion strength.

2.4.5. Dynamic mechanical analysis. The dynamic mechanical analysis (DMA) was conducted using a DMA1 module from Mettler-Toledo, Switzerland, to study the effect of the utilization of the LIG pattern on the thermomechanical properties of the PLA substrate. A dual cantilever beam clamp was used for the DMA test and samples (50 × 10 × 1.5 mm^3) were tested under displacement control mode at the frequency of 1 Hz and oscillatory displacement with an amplitude of 15 μm at a 2 °C min^{-1} heating rate from 30 to 100 °C.

2.5. Evaluation of shape memory and self-sensing performance of LIG/PLA composite

2.5.1. Electrical actuation and deformation sensing. The Joule heating performance of the transferred LIG pattern on the PLA substrate was optimized through a combined theoretical and experimental approach. This optimization enabled the determination of the required electrical power to reach the desired programming temperature of 80 °C (T_g + 20) for shape recovery of the LIG/PLA composite. Two theoretical models were used to estimate the steady-state temperature in the LIG/PLA specimen after applying an AC voltage to LIG: an analytical heat transfer method (eqn S1†) and finite element method (FEM) simulations (details in ESI†). The results from both models were compared with experimental measurements. Experimental optimization was done using a test setup shown in Fig. 2(a) under constant ambient conditions at 25 °C. A custom grip equipped with copper film facilitated connection to a power supply (UNI-T, UDP6720) while maintaining appropriate pressure. The LIG pattern ends were secured with copper adhesive tape (3M 1181) to ensure reliable electrical connections with minimal contact resistance. The experiments explored a range of voltages (15, 20, 25, 30 V) applied for 3 minutes. An infrared thermal camera (FLIR C5) monitored temperature changes on the backside of the LIG/PLA sample

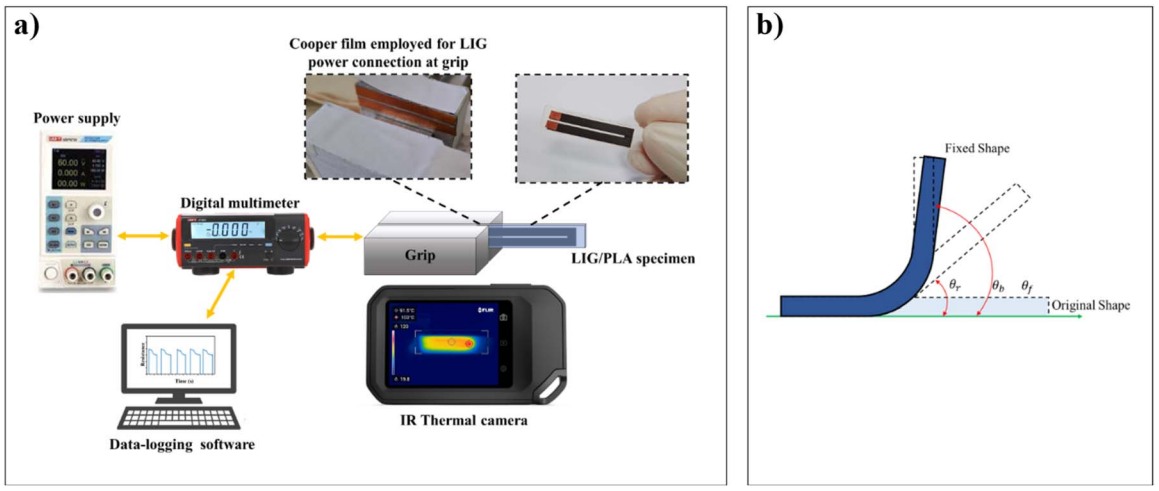

Fig. 2 (a) Schematic of test setup used for shape memory performance experiments. (b) Schematic illustration of LIG/PLA specimen recovery process.

every 5 seconds. Thermal image processing software (ResearchIR, FLIR) calculated the average temperature for each image, enabling investigation of the correlation between applied voltage and resulting temperature rise in the LIG/PLA composite. An emissivity value of 0.95 was used for IR imaging. This value was determined through a calibration process. A K-type thermocouple was used alongside the IR camera to simultaneously record specimen temperatures while heating them on a hotplate. By varying the emissivity between 0.9 and 1, it was found that 0.95 yielded the close temperature correlation between the thermocouple and IR camera for both PLA and LIG/PLA specimens.

The optimized electrical power was utilized to evaluate the shape recovery performance of the LIG/PLA composite actuated electrically. The existing test setup was maintained, incorporating a data-logging multimeter (UNI-T UT803) to monitor current and resistance in the LIG during recovery. The LIG/PLA sample was heated to 80 °C by applying voltage to the LIG pattern. A semi-circular bar (15 mm radius) then bent the sample to a 90° angle, placing the LIG pattern under tension on the convex side. The power was turned off for cooling and shape fixation. Eqn (1) was used to calculate the shape fixity ratio (R_f). Subsequently, power was turned on to induce recovery. Changes in resistance and temperature were recorded using a multimeter and thermal camera, respectively. The entire process was video recorded to measure angle change for calculating the recovery ratio (R_r) using eqn (2). A schematic representation of recovery process is depicted in Fig. 2(b).

$$R_f(\%) = \frac{\theta_f}{\theta_b} \times 100 \quad (1)$$

$$R_r(\%) = \frac{\theta_f - \theta_r}{\theta_f} \times 100 \quad (2)$$

2.5.2. IR light actuation and deformation sensing. The photothermal response of the LIG pattern transferred onto a PLA substrate was investigated by evaluating the temperature changes in PLA and LIG/PLA samples under infrared (IR) light exposure. The samples were positioned 15 cm away from an IR light source and temperature variations were captured on the backside of the specimens. The procedure employed here was same as what described for Joule heating performance in the preceding section, allowing for the determination of the average backside temperature of each specimen over time. An IR bulb served as the light source for the photothermal response experiments. A dimmer controlled the intensity of the IR bulb, allowing for settings of 100%, 75%, 50%, and 25% power. This provided a range of light intensities for the experiments to optimize required IR light intensity to reach a steady-state temperature of 80 °C. A radiometer (model PMA2200, Solar Light Co., Inc.) measured the average light intensity at each power level, resulting in values of 166, 138, 85, and 38 mW cm^{-2}, respectively.

The optimized IR light intensity was employed to evaluate the IR light actuated shape recovery performance of the LIG/PLA composite. The procedure for recording resistance and recovery ratio remained identical. However, instead of applying electric power to the LIG pattern, the IR bulb was employed to heat the LIG/PLA specimen. The same actuation procedure was repeated for pristine PLA specimens, which had previously been fixed at a 90° angle at 80 °C for comparison purposes.

3. Results and discussion

3.1. Produced LIG

The engraving conditions, described in Section 2.2, resulted a uniform LIG pattern on the PI film with the designed dimensions, as shown in Fig. 3(a).

3.2. Fabricated LIG/PLA composite

The LIG pattern initially produced on the PI film by laser engraving was successfully transferred to a PLA substrate using the proposed hot compression transfer technique. This resulted in a LIG/PLA composite, which is shown in Fig. 3(b).

3.3. Characteristics of the LIG/PLA composite

3.3.1. Raman spectroscopy. Raman spectra of LIG before and after transferring onto PLA substrate is shown in Fig. 4. Evidently, the Raman spectrum before transferring exhibited the typical well-resolved D-band (~1350 cm^{-1}), G-band (~1580 cm^{-1}) and symmetrical 2D-band (~2700 cm^{-1}) that can be fitted using one Lorentzian peak of LIG. In comparison, after the transfer process, the 2D-band became almost completely undetectable. The overall profile became more characteristic of amorphous carbon, with broader D- and G-

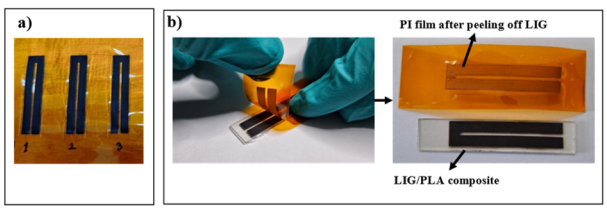

Fig. 3 Digital images of produced (a) LIG pattern (b) LIG/PLA composite specimen.

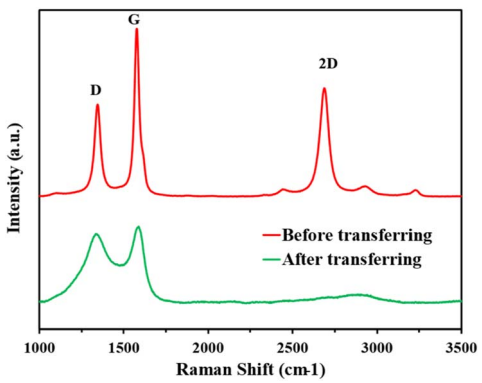

Fig. 4 Raman spectra of LIG before and after transferring to PLA substrate.

bands. This observation in Raman spectra is consistent with previous observations when transferring LIG to other materials.[41] This is because that the transfer process flips the LIG from one side to another. Therefore, the Raman spectra of LIG before and after transferring essentially reflected the characteristics of two sides of LIG with different degree of graphitization. As demonstrated by Mamleyev *et al.*,[42] the reason for this difference in Raman profile of LIG through its thickness is that the upper surface experiences a higher laser irradiation intensity compared to the lower surface near the PI film. Consequently, the upper layer converts more efficiently to LIG, with the layer being less graphitized the closer it is to the PI film.

3.3.2. Morphological characteristics of the LIG. Scanning electron microscopy (SEM) images in Fig. 5(a) depicts the morphology of the LIG on the PI film. The cross-section SEM images showed clearly the formation of LIG with a thickness of approximately 41 ± 6 μm on the top PI film. This LIG layer was readily distinguishable from PI film by its microporous structure. The formation of this microporous structure of graphene flakes was more pronounced in top view SEM images, aligned with the laser scribing direction. Fig. 5(b) illustrates SEM images of LIG after transferring to PLA. the cross-sectional images of LIG/PLA specimens showed a more compact morphology of the LIG with a reduced thickness of 30 ± 7 μm. This compaction likely occurred because of hot compression molding method used for transferring. The top-view SEM image of the transferred LIG, corresponds to the bottom side of the LIG, exhibited this compact structure with a combination of smooth less graphitized LIG regions and porous regions fixed at the PLA's surface. Furthermore, cross-section and top-view SEM images of the PI film after LIG removal (Fig. 5(c)) demonstrated the effectiveness of the transfer method. No residual LIG was observed on the PI surface, which exhibited a bubble-like morphology indicative of boiling or depolymerization of the PI film in deeper sections due to high temperatures during laser engraving.

3.3.3. Sheet resistance measurements. The sheet resistance of LIG was measured before and after transfer to a PLA substrate and results are shown in Fig. 6. The sheet resistance exhibited an increase from 18 ± 0.9 Ω sq^{-1} to 40.3 ± 3.7 Ω sq^{-1} following the transfer process. Two primary reasons likely contribute to this observed increase. Firstly, as explained earlier, the transfer process inherently flips the LIG from one side to another. This resulted in pre- and post-transfer measurements corresponding to distinct LIG surfaces (top and bottom) that has different characteristics as confirmed by Raman spectra and SEM images. Secondly, the hot compression transfer technique might disrupt conductive pathways within the LIG structure by penetration of molten PLA into the LIG microstructure. This

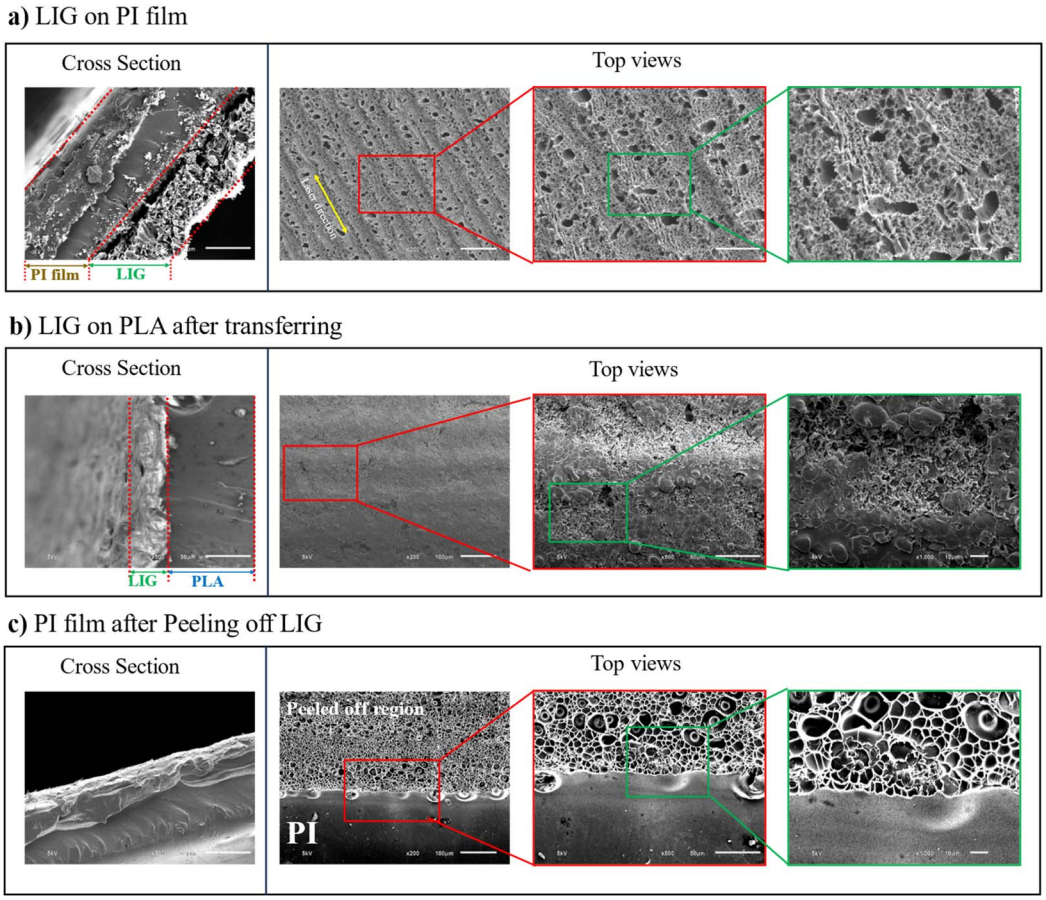

Fig. 5 SEM micrographs of (a) LIG on PI film, (b) LIG after transferring onto PLA, (c) PI film after LIG removal.

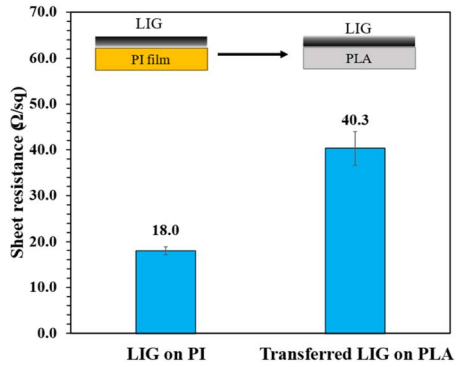

Fig. 6 Sheet resistance of LIG on PI film and after transferring to PLA substrate.

aligns with previously reported findings on transferring LIG to other thermoplastic substrates.[36]

While the sheet resistance increased after transfer (40.3 ± 3.7 Ω sq^{-1}), the resulting LIG still demonstrates adequate conductivity for applications requiring patterned conductivity, such as SMPCs applications. Obviously, this value can be further optimized by controlling laser scribing parameters and compression transferring condition in future works.

3.3.4. Adhesion durability of transferred LIG. Fig. 7(a) shows the results of cyclic peel-off test with Scotch tape on the LIG/PLA composite specimens. As can be seen, the resistance of the LIG remained constant throughout the peel-off cycles. Notably, after each peel-off cycle, no LIG particles were observed adhering to the tape (ESI Video 1†). This finding confirmed the sufficient adhesion of the transferred LIG to the PLA substrate.

3.3.5. Viscoelastic properties of LIG/PLA composite. The storage modulus, loss modulus, and tan δ curves of both pristine PLA and LIG/PLA composite are shown in Fig. 7(b) and (c). As can be seen, the incorporation of LIG on the PLA surface did not significantly affect the storage modulus at 30 °C, with only a reduction of less than 6%. The T_g value of PLA obtained from both tan δ and loss modulus curves was 66 °C and 60 °C, respectively, for both pristine PLA and LIG/PLA samples, demonstrating the independence of the SMP substrate's T_g from the incorporation of LIG onto the surface. This observation aligns well with one of the primary objectives of using LIG as a multifunctional component in SMPC applications.

The difference in T_g values obtained from the loss modulus curve and the tan δ curve is attributed to the distinct aspects of viscoelastic behavior each curve characterizes. The loss modulus curve focuses on energy dissipation and the onset of viscous behavior, while the tan δ curve emphasizes the material's ability to dampen vibrations and dissipate energy.[43] For the purpose of further shape memory experiments in this study, a T_g of 60 °C, obtained from the loss modulus curve, was assumed for both PLA and LIG/PLA composites. The only difference in viscoelastic behavior between PLA and LIG/PLA specimens is the height of the tan δ and loss modulus peaks. Notably, the peaks for the LIG/PLA specimen are smaller. This is likely because the presence of the LIG layer creates a stiffer interface that restricts the mobility of PLA chains. During the glass transition temperature (T_g), these chains normally undergo relaxation processes that contribute to the peak height in tan δ and loss modulus curves. The restricted mobility due to the interface hinders these relaxation processes, resulting in a smaller peak height for the LIG/PLA composite compared to pristine PLA.

3.4. Shape memory and self-sensing performance of the LIG/PLA composite

3.4.1. Electric response and simultaneous deformation sensing. The LIG/PLA specimens exhibited distinct temperature changes when subjected to different voltages, as shown in Fig. 8(a). In resistive joule heating systems, the time constant is defined as the time required to reach a specific level (usually 63.2%) of the final steady-state value. This constant dictates how quickly the system can respond to electrical power input and achieve the steady-state temperature. Therefore, a lower time constant enables a faster temperature rise to T_g, which is essential for accelerating the shape recovery process. As can be seen, regardless of the applied voltage, the temperature increased sharply within the first 30 seconds (correspond to time constant), slowing to reach a steady state after about 2 minutes. Higher voltages accelerated this rise, which is crucial for quickly reaching T_g (60 °C) and programming temperatures (80 °C). At 15 V, neither T_g nor 80 °C was reached, but at 20 V, T_g was attained within 60 seconds. Both T_g and 80 °C were reached with voltages of 25 V and 30 V, with higher voltages significantly reducing the time to reach target temperatures.

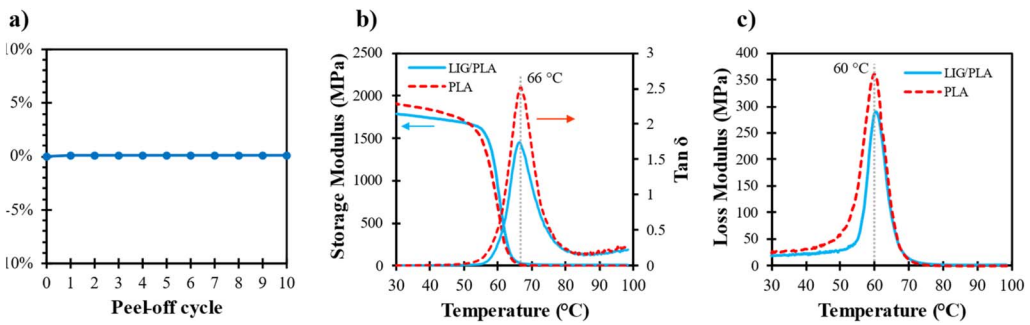

Fig. 7 (a) Resistance changes of transferred LIG under cyclic scotch tape peel-off test (b) storage modulus, tan δ and (c) loss modulus for pristine PLA and LIG/PLA composite.

While achieving recovery temperatures rapidly is crucial for fast recovery of LIG/PLA composite, the maximum temperature reached by the SMP/LIG specimen is equally important. Ideally, this temperature should fall within a range close to the programming temperature (80 °C). Analytical models and finite element simulations estimated the steady-state temperature of the LIG/PLA specimens under various electrical powers, showing close agreement with experimental data, as shown in Fig. 8(b). Additionally, Fig. 8(d) and (e) show the steady-state temperature distributions on the back side of the LIG/PLA specimen, captured by a thermal camera and obtained from FEM simulations, respectively. The temperature distributions exhibit nearly identical profiles, reinforcing the validity of the FEM simulations. Subsequently, an optimum electrical power of 0.95 W was determined according to validated analytical equation (eqn S5†) to ensure having a maximum steady-state temperature of 80 °C during shape recovery in a 1 mm-thick LIG/PLA composite. This optimum value was used in subsequent electrically actuated shape recovery experiments.

In addition to the thermal response of the LIG pattern to different voltages, the variation in LIG resistance over time was recorded to investigate the dynamic change in electrical resistance. The resistance changes over time at different voltages are presented in Fig. 8(c). As shown, a slight decrease in resistance occurred at all voltages due to the corresponding increase in temperature (refer to Fig. 8(a)). Once the temperature reached a steady-state value, the resistance remained constant. An exception was observed at 30 V, where the resistance initially decreased but started to increase after 90 seconds. As mentioned earlier, at 30 V, the steady-state temperature reached 100 °C, causing a reduction in the stiffness of PLA and bending of the sample due to its weight. This led to the stretching of the

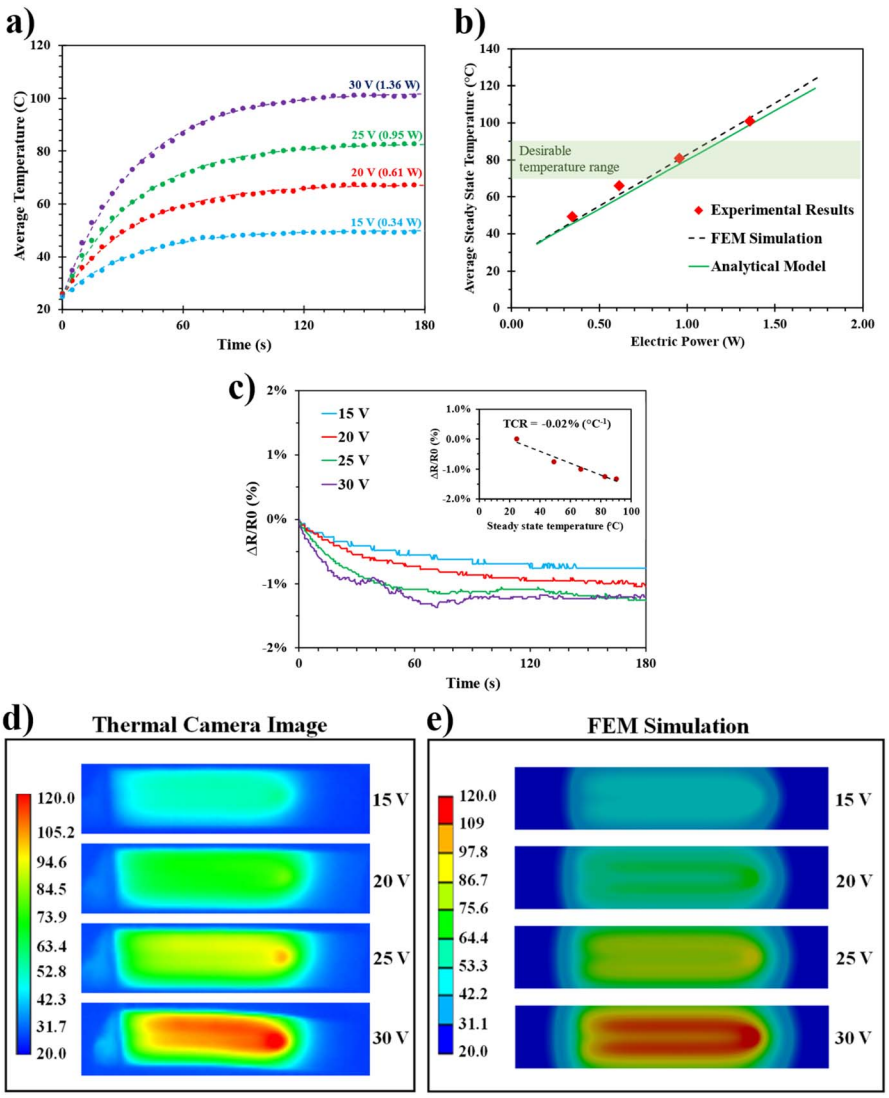

Fig. 8 Joule heating performance of LIG/PLA composite: (a) time-dependent average back-side temperature at different voltages. (b) Steady-state temperature *versus* applied electric power from experiments, FEM simulation, and analytical equation. (c) Time-dependent resistant change of LIG pattern at different voltages and calculated TCR value. (d) Thermal camera images at steady-state temperature for different voltages. (e) Steady-state temperature distribution contours from FEM simulation at different applied voltages.

LIG, which in turn resulted in an increase in resistance. This deformation and bending are also visible in the thermal images at 30 V (Fig. 8(d)). This clearly demonstrates the importance of optimizing the maximum achievable steady-state temperature to avoid undesirable stiffness reduction and deformations.

Additionally, the resistance at each steady-state temperature was used to calculate the temperature coefficient of resistance (TCR) of the transferred LIG. The inset plot in Fig. 8(c) presents the resistance change over temperature, with the slope of the fitted line corresponding to a TCR of -0.02% ($^{\circ}C^{-1}$) in the temperature range of 25 to 90 °C. This TCR resulted in a maximum reduction in resistance of around 1% for an optimum electric power of 0.95 W, which can be considered negligible during electrically actuated shape memory experiments.

Fig. 9 presents the deformation sensing evaluation of the LIG/PLA composite during cyclic electrically actuated shape recovery experiments. Fig. 9(a) shows the piezoresistive response and maximum temperature, with key events annotated during the first cycle of shape fixation and recovery. Corresponding digital and thermal images for each labelled time point are shown in Fig. 9(c). Additionally, the shape recovery of LIG/PLA with electrical actuation is demonstrated in ESI Video 2.†

Initially, applying voltage to the LIG pattern resulted in a temperature rise until the programming temperature was reached at point 1. At this point, the current was turned off, and the specimen was bent to 90° and cooled to approximately 40 °C to fix its temporary shape (point 2). The resistance of the LIG pattern increased to around 800 Ω due to the applied tensile stress on LIG during bending, consistent with the piezoresistive nature of the LIG pattern. When the current was reapplied at point 2, a minor decrease in resistance was observed between points 2 and 3 due to the initial temperature difference and early-stage recovery. The main recovery process began when the temperature reached T_g (60 °C) at point 3, during which resistance decreased as the shape recovered. The recovery rate accelerated significantly when the temperature reached the programming temperature of 80 °C (point 4), continuing until complete recovery at point 5. Fig. 11(b) highlights this by plotting recovery ratio and resistance change ratio over time, showing a steeper slope in the recovery curve at the programming temperature, indicating faster recovery. Additionally, it shows how resistance variation was in a good harmony with

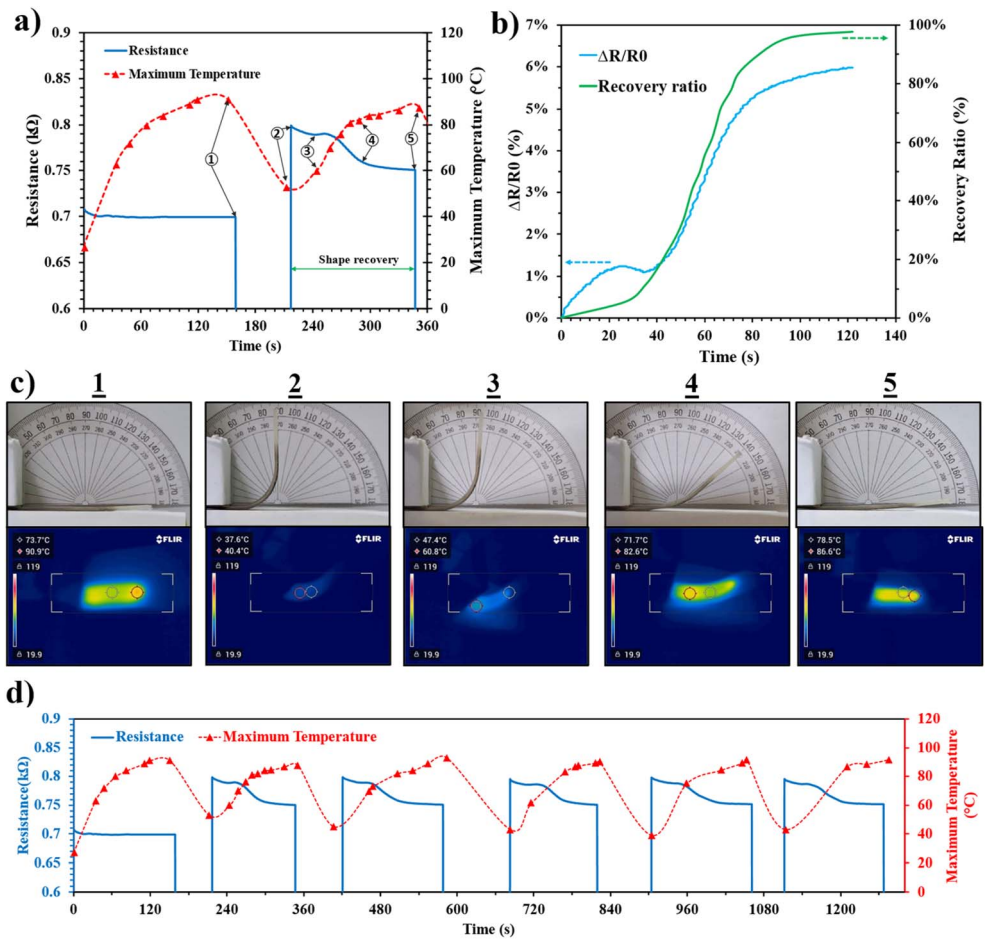

Fig. 9 (a) Time-dependent piezoresistive response and temperature during the first recovery cycle of LIG/PLA with labelling of important time events. (b) Correlation between recovery ratio and resistance change ratio at the first cycle. (c) Digital images (first row) and thermal images (second row) of labelled time events. (d) Piezoresistive response and temperature measurements for five cycles of shape recovery.

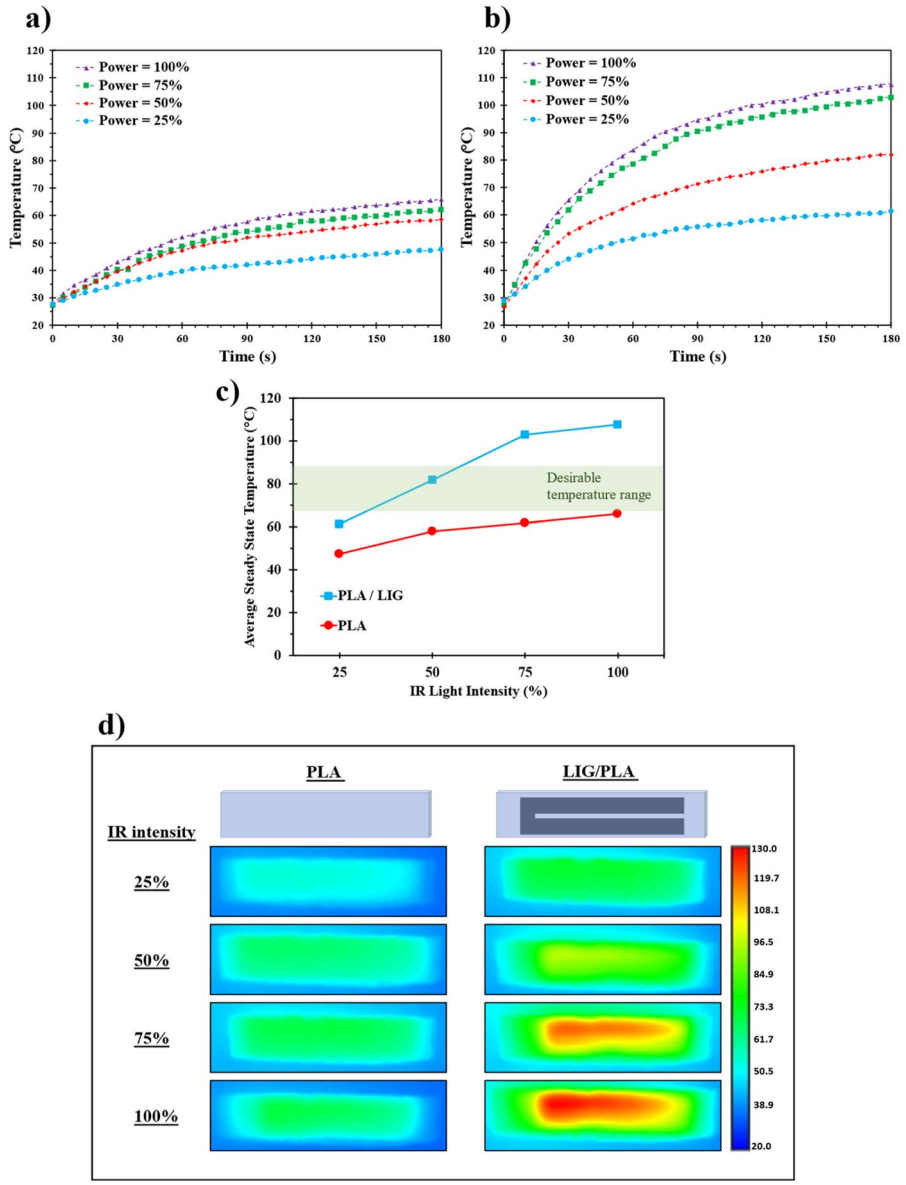

Fig. 10 (a) Rear-surface temperature as a function of time under different IR light intensities for PLA and (b) LIG/PLA specimens. (c) Average equilibrated temperature at rear-surface of specimens *versus* IR light intensity. (d) Thermal camera images after 3 minutes of IR light exposure for PLA and LIG/PLA specimens.

recovery ratio, highlighting self-sensing capability of LIG/PLA composite.

Despite continuous resistance decrease during recovery, the initial pre-bending resistance was not fully recovered due to some irreversible breakage of conductive pathways within the LIG's microporous structure. However, this phenomenon was only noted during the first cycle. Subsequent cycles, as shown in Fig. 9(d), demonstrated complete resistance recovery to the pre-bending value, confirming the stability of the LIG pattern for deformation sensing after the first cycle. Additionally, Fig. 9(d) shows that the maximum temperature remained within the desired range throughout the cyclic recovery process, validating the effectiveness of the developed analytical equation for estimating the required electrical power.

As mentioned earlier, the system's time constant can limit the recovery time of the LIG/PLA composite, and reducing it can lead to faster recovery. Generally, the time constant depends on the characteristics of the LIG pattern, which can be optimized through laser engraving conditions or by adjusting the pattern geometry. It can also be reduced by minimizing heat loss from the LIG to the surroundings by integrating the pattern inside the PLA substrate to create a laminate. These optimizations were beyond the scope of this study and could be the subject of a future detailed investigation. Another strategy to decrease recovery time in practical applications is to employ a varying voltage to control the temperature. By initiating the cycle with a higher voltage and gradually reducing it, we can achieve the desired temperature without exceeding it.

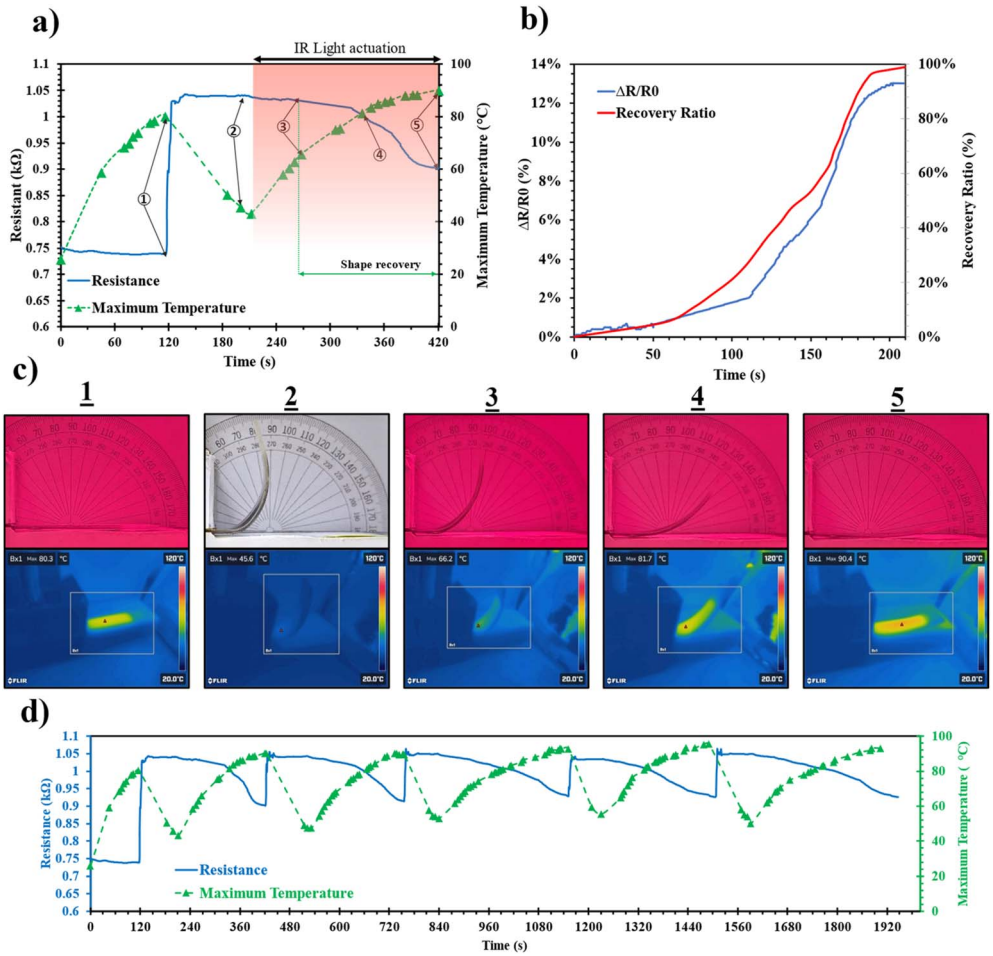

Fig. 11 (a) Time-dependent piezoresistive response and temperature during the first recovery cycle with labelling of important time events. (b) Correlation between recovery ratio and resistance ratio at the first cycle. (c) Digital images (first row) and thermal images (second row) of labelled time events. (d) Piezoresistive response and temperature measurements for five cycles of shape recovery.

3.4.2. IR light response and simultaneous deformation sensing. Fig. 10 (a) and (b) depicts the thermal response of PLA and LIG/PLA specimens subjected to varying IR light intensities. As expected, both materials exhibited a temperature rise with increasing intensity and exposure time. Notably, LIG/PLA specimens consistently displayed a more pronounced temperature increase compared to pristine PLA at all measured time points. This is further emphasized in Fig. 10(c), which illustrates the average steady-state temperature reached by PLA and LIG/PLA specimens after 3 minutes of exposure. For instance, at the highest light intensity (100%), the maximum temperature achieved by PLA was only 65 °C, compared to 107 °C for the LIG/PLA specimen. Fig. 10(d) complements the data by showcasing thermal camera images of PLA and LIG/PLA specimens after 3 minutes of IR light exposure at a specific intensity. The images visually confirmed the more significant temperature increase in LIG/PLA specimens, evident from their warmer appearance compared to PLA. This behavior can be attributed to the superior light absorption of LIG/PLA compared to pristine PLA across the visible and infrared spectrum, as confirmed by UV-VIS-NIR spectroscopy (see Fig. S3 in ESI†), and the inherent ability of LIG to convert this absorbed light into heat due to its photothermal conversion properties.

As previously mentioned, the final equilibrated temperature for heat-responsive SMPs is crucial to obtain a successful recovery of LIG/PLA specimen for ensuring successful recovery of the LIG/PLA specimen without exceeding the programming temperature value. This value should ideally lie around 80 °C. Therefore, an IR bulb power of 50% (85 mW cm^{-2}) appeared to be the optimal setting for LIG/PLA actuation and this value was used for further IR light actuated shape recovery experiments.

Fig. 11 presents the deformation sensing evaluation of the LIG/PLA composite during cyclic IR light actuated shape recovery experiments. Fig. 11(a) presents the piezoresistive response and temperature during the LIG/PLA shape fixation and recovery process, with key events marked. Corresponding digital and thermal images are presented in Fig. 11(c). Fig. 11(b) illustrates the correlation between recovery ratio and resistance change ratio during the IR light-actuated recovery experiment. Additionally, the shape recovery of LIG/PLA with IR light actuation is demonstrated in ESI Video 3.† The results obtained from the IR light actuated recovery experiments exhibited

Table 1 Shape memory performance of LIG/PLA composite

		Electrical actuation		IR light actuation	
Sample	Shape fixity ratio (%)	Recovery ratio (%)	Recovery time (s)	Recovery ratio (%)	Recovery time (s)
PLA	99.1 ± 0.3	NA[a]	NA	0[b]	NA
LIG/PLA	98.9 ± 0.2	98.3 ± 0.47	145 ± 14	98.9 ± 0.35	245 ± 28

[a] Not available. [b] No shape recovery was observed after 3 min at 85 mW cm^{-2} IR exposure.

a remarkable degree of similarity in deformation sensing capability of LIG/PLA composite to those achieved with electrical actuated recovery (refer to Fig. 9 for comparison). This consistency reinforces the LIG pattern's suitability as a deformation sensor during shape memory recovery, independent of the heating mechanism.

However, a slight difference was observed in the shape memory performance of the LIG/PLA composite when actuated electrically or with IR light. Table 1 summarizes the key shape memory parameters for comparison, including shape fixity ratio, shape recovery ratio, and recovery time. Notably, the shape fixity and recovery ratios for the LIG/PLA composite were comparable for both actuation methods and favourably matched values reported for PLA in prior literature.[40] However, the recovery time exhibited significant differences, with IR light actuation taking roughly twice as long as electrical actuation. This discrepancy can be attributed to the inherent heating mechanisms of each method. During electrical actuation, the applied voltage generates heat uniformly throughout the LIG pattern. Conversely, with IR actuation, the LIG pattern absorbs light and converts it into heat, leading to variations in heating rates across the material. Besides the contrasting heating rates and mechanisms, another factor comes into play. At a fixed 90° angle, some portions of the LIG/PLA specimen were parallel to the light direction. This configuration hindered uniform heat generation, resulting in a slower recovery process. However, Fig. 11(b) demonstrates that the recovery rate increases as the angle between the LIG/PLA composite and the light source changes, leading to more efficient heat generation within the LIG pattern.

Furthermore, Table 1 clearly demonstrates the added functionalities imparted to PLA by integrating LIG. The LIG/PLA composite exhibits both electrical- and IR light-responsive shape memory performance, functionalities absent in pristine PLA.

4. Conclusions

This study demonstrates the successful integration of LIG pattern onto PLA substrate using a hot compression method. This method effectively transferred the LIG pattern, creating LIG/PLA composites with the pattern embedded on the PLA surface. The transferred LIG pattern functioned as both Joule heating and photothermal elements. This enabled the actuation of LIG/PLA composite using either electrical or IR light stimuli. Additionally, the LIG pattern exhibited piezoresistive behaviour. This enabled to track the recovery ratio of the LIG/PLA composite throughout the shape recovery process, while concurrently undergoing electrical or IR light actuation. These findings highlight the potential of LIG as a multifunctional component for SMPCs. By integrating LIG patterns, SMPCs gain multi-stimuli responsiveness and self-sensing functionalities. Furthermore, the ability to achieve actuation and deformation sensing using a single, integrated LIG pattern simplifies the fabrication process for developing advanced, multi-responsive SMPCs. These SMPCs have potential applications in various fields, such as self-deployable structures or adaptive materials. Future work can investigate the integration of LIG patterns with different SMP materials. This exploration could lead to a wider range of actuation responses and mechanical properties. Additionally, research can explore more complex LIG patterns and geometries to achieve more controlled and localized actuation within the SMPCs.

Data availability

Data supporting this study are included within the article.

Author contributions

Reza Gholami; conceptualization, methodology, formal analysis; writing & editing. Ibrahim Lawan; methodology, review and editing; Panuwat Luengrojanakul; methodology, review and editing, Sahar Ebrahimi; methodology, conceptualization. Cheol-Hee Ahn; supervision and result validation. Sarawut Rimdusit; supervision, resources, validation, review and editing.

Conflicts of interest

There are no conflicts to declare.

Acknowledgements

We gratefully acknowledge the support and funding provided by the Second Century Fund (C2F) at Chulalongkorn University, the National Research Council of Thailand (NRCT) and Chulalongkorn University (No. 42A660910), and the Thailand Science Research and Innovation Fund Chulalongkorn University (No. 6641/2566). Additionally, we wish to extend our thanks to Prof. Dr Sanong Ekgasit of Department of Chemistry, Faculty of

Science, Chulalongkorn University for letting the team have access to the SEM.

Notes and references

1 H. Bhanushali, S. Amrutkar, S. Mestry and S. T. Mhaske, *Polym. Bull.*, 2021, **79**(6), 3437–3493.
2 F. Zhang, Y. Xia, Y. Liu and J. Leng, *Nanoscale Horiz.*, 2020, **5**, 1155–1173.
3 S. Chen, J. Hu, H. Zhuo, C. Yuen and L. Chan, *Polymer*, 2010, **51**, 240–248.
4 Y. Liu, H. Lv, X. Lan, J. Leng and S. Du, *Compos. Sci. Technol.*, 2009, **69**, 2064–2068.
5 A. Lendlein, H. Jiang, O. Jünger and R. Langer, *Nature*, 2005, **434**(7035), 879–882.
6 W. Jamnongpak, S. Tiptipakorn, H. Arumugam, K. Charoensuk, P. Karagiannidis and S. Rimdusit, *Nanoscale Adv.*, 2024, **6**, 499–510.
7 M. Y. Razzaq, M. Behl and A. Lendlein, *Adv. Funct. Mater.*, 2012, **22**, 184–191.
8 G. Li, G. Fei, H. Xia, J. Han and Y. Zhao, *J. Mater. Chem.*, 2012, **22**, 7692–7696.
9 X. J. Han, Z. Q. Dong, M. M. Fan, Y. Liu, J. H. Li, Y. F. Wang, Q. J. Yuan, B. J. Li and S. Zhang, *Macromol. Rapid Commun.*, 2012, **33**, 1055–1060.
10 Y. Liu, H. Du, L. Liu and J. Leng, *Smart Mater. Struct.*, 2014, **23**, 023001.
11 M. Singh, T. Gulamabbas, B. Ahumuza, N. P. Singh and V. Mishra, *Aerospace Polymeric Materials*, 2022, pp. 189–210.
12 Y. Chen, X. Zhao, Y. Li, Z. Y. Jin, Y. Yang, M. B. Yang and B. Yin, *J. Mater. Chem. C*, 2021, **9**, 5515–5527.
13 J. A. C. Liu, J. H. Gillen, S. R. Mishra, B. A. Evans and J. B. Tracy, *Sci. Adv.*, 2019, **5**(8), eaaw2897.
14 J. Delaey, P. Dubruel, S. Van Vlierberghe, J. Delaey, P. Dubruel and S. Van Vlierberghe, *Adv. Funct. Mater.*, 2020, **30**, 1909047.
15 W. He, D. Zhou, H. Gu, R. Qu, C. Cui, Y. Zhou, Y. Wang, X. Zhang, Q. Wang, T. Wang and Y. Zhang, *Macromol. Rapid Commun.*, 2023, **44**, 2200553.
16 Y. Liu, F. Zhang, J. Leng, K. Fu, X. Lucas Lu, L. Wang, C. Cotton, B. Sun, B. Gu, T.-W. Chou, Y. Liu, B. Sun, B. Gu, K. Fu, X. L. Lu, L. Wang, T. Chou, F. Zhang and J. Leng, *Adv. Mater. Technol.*, 2019, **4**, 1900600.
17 Q. Peng, H. Wei, Y. Qin, Z. Lin, X. Zhao, F. Xu, J. Leng, X. He, A. Cao and Y. Li, *Nanoscale*, 2016, **8**, 18042–18049.
18 F. Guo, X. Zheng, C. Liang, Y. Jiang, Z. Xu, Z. Jiao, Y. Liu, H. T. Wang, H. Sun, L. Ma, W. Gao, A. Greiner, S. Agarwal and C. Gao, *ACS Nano*, 2019, **13**, 5549–5558.
19 X. Gong, L. Liu, Y. Liu and J. Leng, *Smart Mater. Struct.*, 2016, **25**, 035036.
20 W. Jamnongpak, S. Tiptipakorn, H. Arumugam, K. Charoensuk, P. Karagiannidis and S. Rimdusit, *Nanoscale Adv.*, 2024, **6**, 499–510.
21 C. Cai, Y. Zhang, M. Li, Y. Chen, R. Zhang, X. Wang, Q. Wu, T. Chen and P. Sun, *RSC Adv.*, 2018, **8**, 1225–1231.
22 Y. Liu, G. Zhu, W. Liu, H. Liu, Y. Huo, T. Ren and X. Hou, *Smart Mater. Struct.*, 2018, **27**, 095008.
23 Z. Xu, C. Ding, D. W. Wei, R. Y. Bao, K. Ke, Z. Liu, M. B. Yang and W. Yang, *ACS Appl. Mater. Interfaces*, 2019, **11**, 30332–30340.
24 G. Tian, G. Zhu, S. Xu and T. Ren, *Smart Mater. Struct.*, 2019, **28**, 105006.
25 S. Ishii, K. Uto, E. Niiyama, M. Ebara and T. Nagao, *ACS Appl. Mater. Interfaces*, 2016, **8**, 5634–5640.
26 J. Lin, Z. Peng, Y. Liu, F. Ruiz-Zepeda, R. Ye, E. L. G. Samuel, M. J. Yacaman, B. I. Yakobson and J. M. Tour, *Nat. Commun.*, 2014, **5**(1), 1–8.
27 I. Lawan, P. Luengrojanakul, K. Charoensuk, H. Argunam, C. H. Ahn and S. Rimdusit, *Nanoscale Adv.*, 2024, **6**, 1556–1564.
28 K. K. Mentel, J. Manninen, V. M. Hiltunen, P. Myllyperkiö, A. Johansson and M. Pettersson, *Nanoscale Adv.*, 2021, **3**, 1431–1442.
29 J. Rodrigues, J. Zanoni, G. Gaspar, A. J. S. Fernandes, A. F. Carvalho, N. F. Santos, T. Monteiro and F. M. Costa, *Nanoscale Adv.*, 2019, **1**, 3252–3268.
30 Y. Huang, L. Q. Tao, J. Yu, K. Zheng, G. Wang and X. Chen, *IEEE Electron Device Lett.*, 2020, **41**, 501–504.
31 I. Naseri, M. Ziaee, Z. N. Nilsson, D. R. Lustig and M. Yourdkhani, *ACS Omega*, 2022, **7**, 3746–3757.
32 N. H. Barbhuiya, U. Misra and S. P. Singh, *ACS Appl. Nano Mater.*, 2022, **5**, 10991–11002.
33 Q. Wang, Y. C. Zhang, H. B. Sun, W. K. Zou, N. De Miao, S. L. Liu, Y. H. Jiao, Y. Q. Liu and D. D. Han, *IEEE Photonics Technol. Lett.*, 2023, **35**, 1167–1170.
34 Y. Peng, W. Zhao, F. Ni, W. Yu and X. Liu, *ACS Nano*, 2021, **15**, 19490–19502.
35 H. Liu, K. Chen, R. Wu, S. Pan and C. Zhang, *ACS Appl. Mater. Interfaces*, 2023, **15**, 46550–46558.
36 J. T. Li, M. G. Stanford, W. Chen, S. E. Presutti and J. M. Tour, *ACS Nano*, 2020, **14**, 7911–7919.
37 T. Raza, M. K. Tufail, A. Ali, A. Boakye, X. Qi, Y. Ma, A. Ali, L. Qu and M. Tian, *ACS Appl. Mater. Interfaces*, 2022, **14**, 54170–54181.
38 W. Wang, L. Lu, Z. Li, L. Lin, Z. Liang, X. Lu and Y. Xie, *ACS Appl. Mater. Interfaces*, 2022, **14**, 1315–1325.
39 A. F. Carvalho, A. J. S Fernandes, C. Leitão, J. Deuermeier, A. C. Marques, R. Martins, E. Fortunato, F. M. Costa, A. F. Carvalho, A. J. S Fernandes, C. Leitão, F. M. Costa, J. Deuermeier, A. C. Marques, R. Martins and E. Fortunato, *Adv. Funct. Mater.*, 2018, **28**, 1805271.
40 R. B. da Cunha, S. N. Cavalcanti, P. Agrawal, G. de Figueiredo Brito and T. J. A. de Mélo, *J. Appl. Polym. Sci.*, 2023, **140**, e54561.
41 T. Pinheiro, R. Correia, M. Morais, J. Coelho, E. Fortunato, M. G. F. Sales, A. C. Marques and R. Martins, *ACS Nano*, 2022, **16**, 20633–20646.
42 E. R. Mamleyev, S. Heissler, A. Nefedov, P. G. Weidler, N. Nordin, V. V. Kudryashov, K. Länge, N. MacKinnon and S. Sharma, *npj Flexible Electron.*, 2019, **3**, 1–11.
43 J. D. Ferry, *Viscoelastic Properties of Polymers*, John Wiley & Sons, Canada, 1980.